

Quasinormal ringing and Unruh-Verlinde temperature of the Frolov Black Hole

Akshat Pathrikar^{1,*}

¹*International Centre for Space and Cosmology, Ahmedabad University, Ahmedabad 380009, Gujarat, India*

In this study, we investigate electromagnetic and Dirac field axial-perturbations of a charged regular black hole arising from quantum gravity effects, commonly referred to as the Frolov black hole, a regular (nonsingular) black hole solution. We derive the master wave equations for massless electromagnetic and Dirac perturbations and solve them using the standard Wentzel-Kramers-Brillouin (WKB) method along with Padé Averaging. From these solutions, we extract the dominant and overtone quasinormal mode (QNM) frequencies along with the associated grey-body factors, highlighting the deviations introduced by quantum gravity corrections compared to the classical case of Reissner–Nordström black hole. Furthermore, we analyze the Unruh-Verlinde temperature of this spacetime, providing quantitative estimates of how quantum gravity effects influence both quasinormal ringing and particle emission in nonsingular black hole models.

Keywords : Quasinormal modes, Regular Black Holes, Unruh Temperature, WKB method.

I. INTRODUCTION

The General Theory of Relativity (GR), our modern understanding of gravitation, has enjoyed remarkable success for over a century, passing numerous experimental and observational tests with great precision. Nevertheless, under certain extreme conditions, GR predicts its own breakdown. For instance, the celebrated singularity theorems of R. Penrose and S.W. Hawking [1, 2] demonstrate that spacetime singularities are inevitable within black holes. In these regimes, quantum effects cannot be neglected, signaling that classical GR is no longer sufficient. It is also known that at high densities of matter, quantum effects become important, and the matter pressure may be able to counterbalance gravitational collapse, and it seems reasonable that when matter reaches Planck density, which is the onset of quantum gravity effects, and there would be enough pressure as to prevent the formation of a singularity. This situation has motivated the derivation and study of non-singular or regular black holes.

The question of how general relativity might avoid the formation of spacetime singularities is both long standing and of more than purely formal interest. In 1968, Bardeen presented the first example of a regular black hole—a spacetime with an event horizon but free of sin-

gularities, while still obeying the weak energy conditions [3]. Although conceptually important, Bardeen’s solution lacked for many years a clear physical interpretation because it is not a vacuum solution of Einstein’s equations. To obtain it, one must either introduce some form of external matter or consider modifications to gravity. In fact, Bardeen achieved this geometry by positing an ad hoc stress–energy tensor that is finite everywhere, falls off at infinity, and satisfies the weak energy conditions. Bardeen’s construction inspired numerous subsequent models exploring the mechanisms by which singularities might be avoided. Several alternative regular black hole solutions have since appeared in the literature, particularly within theories where gravity couples to nonlinear electrodynamics [4, 5]. Notably, Dymnikova proposed a black hole whose interior is described by a de Sitter core smoothly matching a Schwarzschild exterior [6]. Further developments and variations of regular black-hole spacetimes have continued to be investigated in many works [7–10].

Regular black holes can be broadly grouped according to the geometry near their center: those featuring a de Sitter (dS) core and those with a Minkowski-like core. Well-known dS-core solutions include the Bardeen black hole, the Hayward black hole [11], and the Frolov black hole [12]. In contrast, regular black holes with a Minkowskian interior are typically described using exponential-type potentials, as discussed in Refs. [13–21].

V. L. Frolov constructed several metrics under a set of intuitive assumptions aimed at finding non-singular

* akshatpathrikar014@gmail.com

black-hole geometries without altering general relativity itself. Extending his analysis to the charged case, Frolov introduced variants such as a modified Hayward solution. In his framework, a characteristic length parameter α_0 (denoted l in the original paper) is tied to a critical energy scale μ through $\alpha_0 = \mu^{-1}$. Thus, alongside the black hole mass, the parameter α_0 sets the scale at which departures from Einstein's equations become important. More precisely, this scale is reached when α_0^{-2} is comparable to the curvature scalar R . Frolov also argued that one may continue to employ the usual metric tensor $g_{\mu\nu}$, while acknowledging a separate quantum-gravity length λ , significantly smaller than α_0 , where such effects dominate. These considerations ensure that the resulting spacetime remains regular even at $r = 0$.

In this work, our goal is to investigate some of the fundamental observable characteristics of quantum-corrected black holes. One of the most important such characteristics is the spectrum of quasinormal modes, these are the damped oscillations that dominate the ringdown phase of a perturbed spacetime at intermediate to late times [22, 23]. These frequencies are often referred to as the “fingerprints” of a black hole, as they are independent of the specific perturbation that excites them and depend entirely on the underlying geometry of the spacetime. Another essential quantity we study is the set of grey-body factors, which determine the fraction of Hawking radiation that can tunnel through the black hole's effective potential barrier and propagate to infinity, which might be detected by a distant observer [24–26]. We also study the Unruh temperature, which arises due to the response of an accelerating observer in a vacuum. An observer undergoing constant acceleration perceives the vacuum as a thermal bath of particles with a characteristic temperature and in the context of black holes, the Unruh temperature serves as a local notion of temperature near the horizon proportional to their acceleration [27, 28]. These quantities provide critical information about the near-horizon geometry and the nature of quantum corrections. Besides, from an observational perspective, most current experimental data arise from the detection of gravitational waves emitted by coalescing black holes and from electromagnetic observations of their surrounding environments. However, both approaches still leave a wide parameter space open

for the interpretation of black hole near-horizon physics, as these regimes remain poorly constrained and subject to significant uncertainties.

The stability of Frolov black holes has previously been investigated by computing QNMs under scalar perturbations [29]. In [30], the authors investigated the properties of QNMs for a probe massless scalar field in the background of Frolov BH in the eikonal limit. In this work, we aim to extend this analysis to electromagnetic and Dirac field perturbations, examining both the fundamental quasinormal mode and the first overtone during the ringdown phase. In addition, we compute the associated greybody factors, which quantify the transmission probability of Hawking radiation through the black hole's effective potential barrier and directly influence its emission spectrum. Such a comprehensive analysis provides deeper insights into the near-horizon geometry and potential quantum gravity effects encoded in the QNM spectrum. More importantly, the possibility of detecting quasinormal ringing signatures from black holes has been proposed in the context of future space-based gravitational-wave observatories, such as LISA, which will be capable of probing these frequencies with high precision as discussed in [31, 32]. Consequently, our results may offer a window into testing quantum gravity corrections to black hole spacetimes through gravitational wave observations.

The paper has been organized in the following manner: In Section (II), we describe the Frolov Black Hole metric, in Section (III), we work out the axial type perturbation equations for the electromagnetic and Dirac field cases, in Section (IV) we describe the WKB method and compute the QNM frequencies for the given perturbations in Tables (I) to (VIII). In Section (V) we compute the grey-body factors associated with the Frolov BH and in Section (VI) we work out the Unruh-Verlinde temperature and compare how quantum corrections modify the standard results.

II. THE FROLOV BLACK HOLE METRIC

A Frolov black hole can be viewed as a charged extension of the Hayward BH, first proposed in Ref. [12]. Its

spacetime geometry is given by

$$ds^2 = -f(r) dt^2 + \frac{dr^2}{f(r)} + r^2 d\theta^2 + r^2 \sin^2 \theta d\phi^2, \quad (1)$$

where

$$f(r) = 1 - \frac{(2Mr - q^2)r^2}{r^4 + (2Mr + q^2)\alpha_0^2}, \quad (2)$$

with M the black-hole mass. The central region of a Frolov BH behaves as if it were endowed with an effective cosmological constant $\Lambda = 3/\alpha_0^2$, where α_0 represents the Hubble length. This Hubble length functions as a form of “universal hair” and is subject to the bound [11]

$$\alpha_0 \leq \sqrt{\frac{16}{27}}M. \quad (3)$$

Meeting this condition implies that quantum-gravity effects become significant. For convenience we set $M = 1$ in what follows, with no loss of generality.

The charge parameter q introduces a specific black-hole “hair” and satisfies $0 \leq q \leq 1$. When $q = 0$, the Frolov BH reduces to the Hayward solution, whereas setting $\alpha_0 = 0$ recovers the Reissner–Nordström (RN) geometry. If both $q = 0$ and $\alpha_0 = 0$, the metric further simplifies to the Schwarzschild solution.

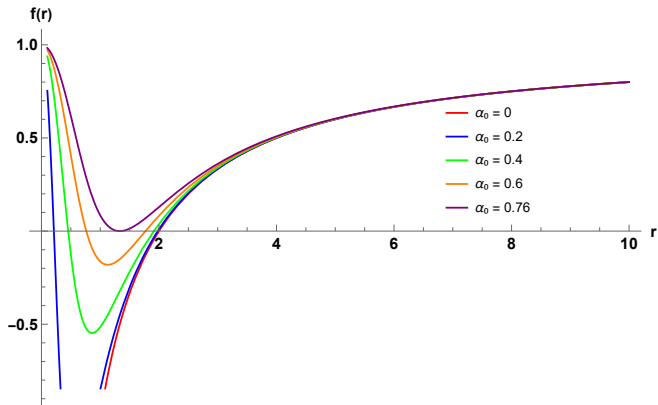


FIG. 1. The metric function $f(r)$ as a function of r for various values of α_0 and with a fixed $q = 0$ Increasing α_0 shifts the curve upward and modifies the horizon structure.

Figures 1, 2, 3 illustrate the metric function $f(r)$ for various choices of q and α_0 . As an example, consider $q = 0$, which corresponds to the Hayward BH. Starting from the Schwarzschild case and increasing α_0 , the Hayward geometry develops a pair of horizons. Further increasing α_0 up to the upper limit given by Eq. (3) leads to the formation of a black hole with double horizons.

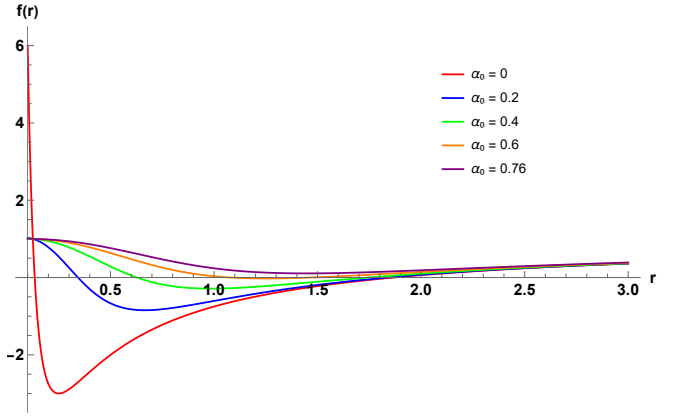


FIG. 2. The metric function $f(r)$ as a function of r for various values of α_0 and with a fixed $q = 0.5$ Increasing α_0 shifts the curve upward and modifies the horizon structure.

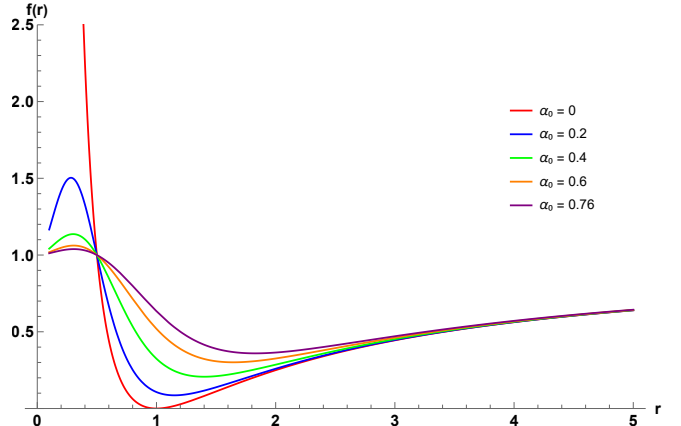


FIG. 3. The metric function $f(r)$ as a function of r for various values of α_0 and with a fixed $q = 1$ Increasing α_0 shifts the curve upward and modifies the horizon structure.

III. THE AXIAL PERTURBATION EQUATIONS

Since we are working with axial perturbations, we present below the field equations for the electromagnetic and Dirac field perturbations in the given curved background.

The general covariant equation for an electromagnetic field is given by

$$\frac{1}{\sqrt{-g}} \partial_\mu (F_{\rho\sigma} g^{\rho\nu} g^{\sigma\mu} \sqrt{-g}) = 0, \quad (4)$$

where $F_{\rho\sigma} = \partial_\rho A_\sigma - \partial_\sigma A_\rho$ and A_μ is the electromagnetic four-potential.

The vector potential A_μ can be expanded in terms of four-dimensional vector spherical harmonics (see Ref. [33]) as

$$A_\mu(t, r, \theta, \phi) = \sum_{\ell, m} \left[\begin{pmatrix} 0 \\ 0 \\ a_{\ell m}(t, r) \sin^{-1} \theta \partial_\phi Y_{\ell m} \\ -a_{\ell m}(t, r) \sin \theta \partial_\theta Y_{\ell m} \end{pmatrix} + \begin{pmatrix} f_{\ell m}(t, r) Y_{\ell m} \\ h_{\ell m}(t, r) Y_{\ell m} \\ k_{\ell m}(t, r) \partial_\theta Y_{\ell m} \\ k_{\ell m}(t, r) \partial_\phi Y_{\ell m} \end{pmatrix} \right], \quad (5)$$

where ℓ is the angular quantum number and m is the azimuthal number. The first column has parity $(-1)^{\ell+1}$ and the second has parity $(-1)^\ell$.

After separation of variables, the perturbation equations reduce to a Schrödinger-like wave equation of the form

$$\frac{d^2 \Psi_{\text{EM}}}{dr_*^2} + [\omega^2 - V_{\text{EM}}(r_*)] \Psi_{\text{EM}} = 0, \quad (6)$$

where r_* is the tortoise coordinate. The effective potential for electromagnetic perturbations is given by

$$V_{\text{EM}}(r) = f(r) \frac{\ell(\ell+1)}{r^2}. \quad (7)$$

Similarly, we work out the field equations for the Dirac perturbations. For a general curved background space-time, the massless Dirac equation reads

$$\gamma^a e_a^\mu (\partial_\mu + \Gamma_\mu) \Psi = 0, \quad (8)$$

where γ^a are the Dirac matrices, e_a^μ is the inverse of the tetrad e_μ^a with $g_{\mu\nu} = \eta_{ab} e_\mu^a e_\nu^b$, and η_{ab} is the Minkowski metric. The spin connections Γ_μ are given by

$$\Gamma_\mu = \frac{1}{8} [\gamma^a, \gamma^b] e_a^\nu e_{b\nu;\mu}, \quad e_{b\nu;\mu} = \partial_\mu e_{b\nu} - \Gamma_{\mu\nu}^\alpha e_{b\alpha} \quad (9)$$

To separate the Dirac equation, we choose the tetrad

$$e_\mu^a = \text{diag} \left(\sqrt{f}, \frac{1}{\sqrt{f}}, r, r \sin \theta \right). \quad (10)$$

Substituting this tetrad into Eq. (8), the Dirac equation becomes

$$\begin{aligned} \gamma^0 \sqrt{f} \frac{\partial \psi}{\partial t} + \sqrt{f} \gamma^1 \left(\frac{\partial}{\partial r} + \frac{1}{r} + \frac{1}{4f} \frac{df}{dr} \right) \psi \\ + \frac{\gamma^2}{r} \left(\frac{\partial}{\partial \theta} + \frac{1}{2} \cot \theta \right) \psi + \frac{\gamma^3}{r \sin \theta} \frac{\partial \psi}{\partial \phi} = 0 \end{aligned} \quad (11)$$

Defining the rescaled perturbation $\psi = f^{-1/4} \phi$, the equation becomes

$$\begin{aligned} \gamma^0 \sqrt{f} \frac{\partial \phi}{\partial t} + \sqrt{f} \gamma^1 \left(\frac{\partial}{\partial r} + \frac{1}{r} \right) \phi \\ + \frac{\gamma^2}{r} \left(\frac{\partial}{\partial \theta} + \frac{1}{2} \cot \theta \right) \phi + \frac{\gamma^3}{r \sin \theta} \frac{\partial \phi}{\partial \phi} = 0 \end{aligned} \quad (12)$$

The Pauli matrices σ_i are defined as

$$\sigma_1 = \begin{pmatrix} 0 & 1 \\ 1 & 0 \end{pmatrix}, \quad \sigma_2 = \begin{pmatrix} 0 & -i \\ i & 0 \end{pmatrix}, \quad \sigma_3 = \begin{pmatrix} 1 & 0 \\ 0 & -1 \end{pmatrix}. \quad (13)$$

Introducing the tortoise coordinate

$$r_* = \int \frac{dr}{f(r)}, \quad (14)$$

and the ansatz for the Dirac spinor

$$\phi(t, r, \theta, \varphi) = \begin{pmatrix} i \frac{G^{(\pm)}(r)}{r} \chi_{jm}^\pm(\theta, \varphi) \\ \frac{F^{(\pm)}(r)}{r} \chi_{jm}^\mp(\theta, \varphi) \end{pmatrix} e^{-i\omega t}, \quad (15)$$

where χ_{jm}^\pm are spinor spherical harmonics given by

$$\chi_{jm}^+ = \begin{pmatrix} \sqrt{\frac{j+m}{2j}} Y_\ell^{m-1/2} \\ \sqrt{\frac{j-m}{2j}} Y_\ell^{m+1/2} \end{pmatrix}, \quad j = \ell + \frac{1}{2}, \quad (16)$$

and

$$\chi_{jm}^- = \begin{pmatrix} \sqrt{\frac{j+1-m}{2j+2}} Y_\ell^{m-1/2} \\ -\sqrt{\frac{j+1+m}{2j+2}} Y_\ell^{m+1/2} \end{pmatrix}, \quad j = \ell - \frac{1}{2}. \quad (17)$$

Here $Y_\ell^{m\pm 1/2}(\theta, \varphi)$ are the usual spin-weighted spherical harmonics.

$$\begin{aligned} & \left(-i \begin{pmatrix} \frac{\partial}{\partial \theta} + \frac{1}{2} \cot \theta & \frac{1}{\sin \theta} \frac{\partial}{\partial \varphi} \\ -\frac{1}{\sin \theta} \frac{\partial}{\partial \varphi} & -\left(\frac{\partial}{\partial \theta} + \frac{1}{2} \cot \theta \right) \end{pmatrix} \right) \begin{pmatrix} \chi_{jm}^\pm \\ \chi_{jm}^\mp \end{pmatrix} \\ & = i \begin{pmatrix} k_\pm & 0 \\ 0 & k_\pm \end{pmatrix} \begin{pmatrix} \chi_{jm}^\pm \\ \chi_{jm}^\mp \end{pmatrix}. \end{aligned} \quad (18)$$

Thus, eqn.(12) can be written in a simplified manner as:

$$\begin{aligned} & \left[\begin{pmatrix} 0 & -\omega \\ \omega & 0 \end{pmatrix} \begin{pmatrix} F^\pm \\ G^\pm \end{pmatrix} - \frac{\partial}{\partial r_*} \begin{pmatrix} F^\pm \\ G^\pm \end{pmatrix} \right. \\ & \left. + \sqrt{f} \begin{pmatrix} \frac{k_\pm}{r} & 0 \\ 0 & -\frac{k_\pm}{r} \end{pmatrix} \begin{pmatrix} F^\pm \\ G^\pm \end{pmatrix} \right] = 0. \end{aligned} \quad (19)$$

The cases (+) and (−) in the functions can be put together after some matching, and the equation can be decoupled as

$$\frac{d^2F}{dr_*^2} + (\omega^2 - V_1) F = 0, \quad (20)$$

$$\frac{d^2G}{dr_*^2} + (\omega^2 - V_2) G = 0. \quad (21)$$

After separation of variables, the Dirac equation reduces to a Schrödinger-like wave equation of the form

$$\frac{d^2\Psi_s}{dr_*^2} + [\omega^2 - V_s(r)] \Psi_s = 0, \quad (22)$$

where r_* is the tortoise coordinate and $V_s(r)$ is the effective potential for the Dirac perturbation. In our case, the potential takes the form

$$V_{\pm 1/2}(r) = \sqrt{f} \frac{|k|}{r^2} \left(|k| \sqrt{f} \pm \frac{r}{2} \frac{df}{dr} \mp f \right), \quad (23)$$

where $|k| = 1, 2, 3, \dots$ is the total angular momentum quantum number. As shown in Ref. [34], for a generic spherically symmetric spacetime, the two potentials $V_{+1/2}(r)$ and $V_{-1/2}(r)$ are isospectral, i.e., they yield identical quasinormal mode spectra.

In our analysis, we therefore work exclusively with $V_{+1/2}(r)$, which is also more convenient for semi-analytic methods such as the WKB approximation.

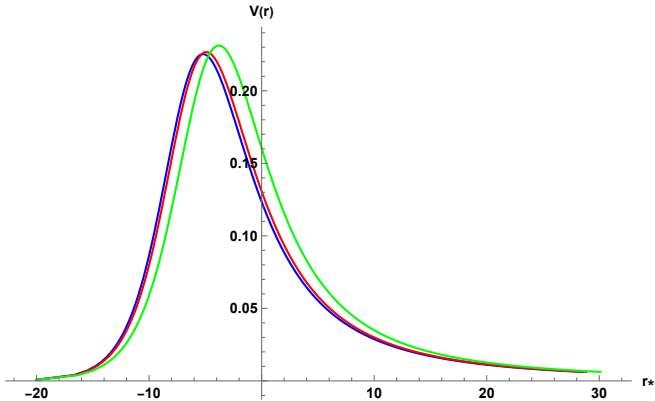


FIG. 4. The variation of $V(r)$ with the tortoise coordinate r_* for varying values of $\alpha_0 = 0$ (red), 0.2 (blue), 0.4 (green), 0.76 (purple) taking $q = 0.2$, $l = 2$, $M = 1$ for the massless electromagnetic perturbations.

IV. WKB METHOD AND QNM FREQUENCIES

To compute the quasinormal mode frequencies and analyze the stability of the Frolov black hole under axial

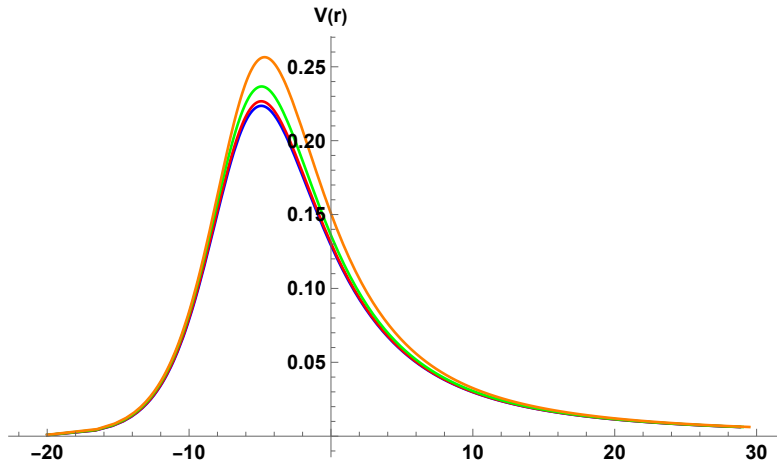


FIG. 5. The variation of $V(r)$ with the tortoise coordinate r_* for different values of $q = 0$ (red), 0.3 (blue), 0.6 (green) with fixed angular momentum number $l = 2$, and $\alpha_0 = 0.2$ for the massless electromagnetic perturbations, taking $M = 1$.

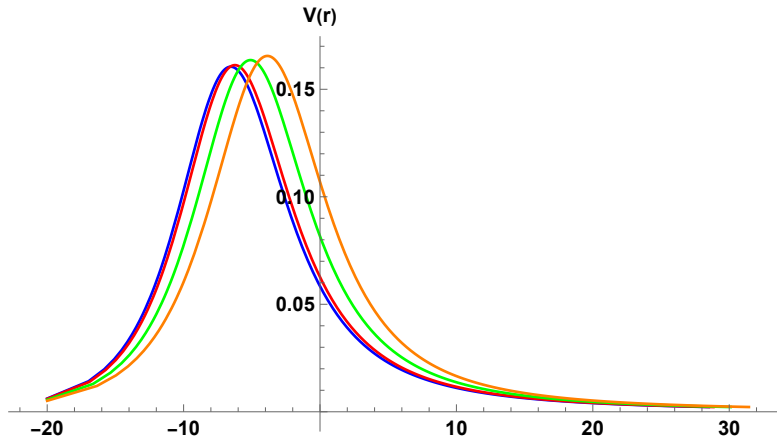


FIG. 6. The variation of $V(r)$ with the tortoise coordinate r_* for the Dirac field perturbations with $|k| = 2$ and varying $\alpha_0 = 0$ (red), 0.2 (blue), 0.4 (green), 0.5 (orange) and $M = 1$.

perturbations, we use the WKB approximation. This semi-analytic technique is particularly well-suited for potentials with a barrier-like structure, as is the case here, where the Regge–Wheeler (RW) potential governs the evolution of axial perturbations (see Fig. 4, 5, 6, and 7). The QNMs are the complex eigenfrequencies of spacetime perturbations: their real part represents the oscillation frequency, while the imaginary part encodes the damping rate of the perturbation.

The evolution of axial gravitational perturbations in the Frolov BH background is governed by the master

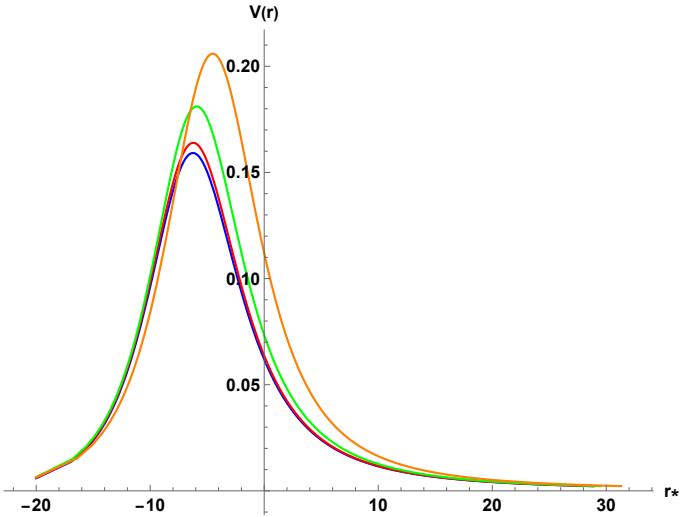


FIG. 7. The variation of $V(r)$ with the tortoise coordinate r_* for the Dirac field perturbations with $|k| = 2$, considering different values of $q = 0$ (red), 0.3 (blue), 0.6 (green), 0.8 (orange), and $\alpha = 0.2$, $M = 1$.

equation,

$$\frac{d^2\psi}{dx^2} + Q(x)\psi = 0, \quad (24)$$

where x is the tortoise coordinate r_* , and $Q(x)$ is defined as

$$Q(x) = \omega^2 - V_{\text{eff}}(r_*). \quad (25)$$

The functional form of $Q(x)$ dictates whether perturbations decay (implying stability) or grow over time, making its accurate modeling crucial for probing the dynamical behavior of the perturbed spacetime.

The Schrödinger-like equation in curved spacetime was first solved using the WKB method by Schutz and Will in 1985 [35]. Iyer and Will subsequently extended the formalism to third order in 1987 [36], significantly improving its precision. Later, Konoplya extended the method up to sixth order [37], and more recently, Matyjasek and Opala pushed the approximation to the thirteenth order [38]. While higher-order WKB schemes typically increase accuracy, they may also introduce numerical instabilities. In particular, results obtained at very high orders, such as the thirteenth, sometimes deviate significantly from those at lower orders due to error amplification and lack of convergence [39].

In this work, we focus primarily on the sixth and eighth order WKB approximations, which strike a good balance between accuracy and computational simplicity.

The sixth-order WKB approximation is expressed as

$$i \frac{\omega^2 - V_0}{\sqrt{-2V_0''}} = \sum_{i=2}^6 \Lambda_i, \quad (26)$$

where $n = 0, 1, 2, \dots$ represents the overtone number.

Higher-order WKB formulations, such as the seventh and eighth orders, incorporate increasingly large numbers of terms—616 for Λ_7 and 1,215 for Λ_8 —making direct computation cumbersome. Nevertheless, they have been shown to yield improved agreement with full numerical solutions in many cases.

Boundary conditions: The computation of QNM frequencies reduces to solving an eigenvalue problem for the perturbation equation, subject to well-defined boundary conditions. These conditions are chosen to represent a physically meaningful response of the spacetime to a transient disturbance. Therefore, we impose

$$\psi(r_*) \sim e^{\pm i\omega r_*}, \quad r_* \rightarrow \pm\infty, \quad (27)$$

where r_* is the tortoise coordinate. The choice $e^{+i\omega r_*}$ at $r_* \rightarrow +\infty$ corresponds to a purely outgoing wave at spatial infinity, while $e^{-i\omega r_*}$ at $r_* \rightarrow -\infty$ represents a purely ingoing wave at the event horizon. Physically, these conditions encode the idea that no radiation can emerge from behind the horizon and that all perturbations detected far away are purely outgoing. They describe the characteristic “ringdown” stage of a black hole’s response, i.e, the phase that follows after any external source of perturbation has ceased [41].

However, the presence of extremely large higher-order terms can lead to numerical instabilities, as observed for the twelfth-order approximation. Our analysis shows that for the electromagnetic and the Dirac perturbation case, we have employed the sixth-order WKB approximation. To ensure numerical consistency, we have also cross-checked our results with higher-order values as well as the Padé Averaged results [42], specifically the eighth-order for the electromagnetic, and for the Dirac case. The outcomes from different orders are found to be in good agreement across all the considered values of the parameters in the metric. In this work, we implement the WKB formalism using the publicly available numerical package developed by R.A. Konoplya [40].

TABLE I. Quasinormal mode frequencies ω for the massless electromagnetic field perturbations for the fundamental mode ($n = 0$), obtained using the 6th and 8th order WKB methods with Padé Averaging for various values of q and α_0 . We set $M = 1$ and $l = 2$.

q	α_0	6th order WKB (Padé), ($n = 0$)		8th order WKB (Padé), ($n = 0$)	
		$Re(\omega)$	$Im(\omega)$	$Re(\omega)$	$Im(\omega)$
0.0	0.0	0.457595	$-0.0950048i$	0.457594	$-0.0950038i$
0.2	0.0	0.460828	$-0.0952257i$	0.460828	$-0.0952258i$
0.2	0.1	0.461245	$-0.0950674i$	0.461245	$-0.0950674i$
0.4	0.2	0.473106	$-0.0950677i$	0.473106	$-0.0950678i$
0.6	0.3	0.496867	$-0.0939648i$	0.496867	$-0.093965i$
0.8	0.4	0.54452	$-0.084335i$	0.544521	$-0.0843349i$

TABLE II. Quasinormal mode frequencies ω for the massless electromagnetic field perturbations for the first overtone ($n = 1$), obtained using the 6th and 8th order WKB methods with Padé Averaging for various values of q and α_0 . We set $M = 1$ and $l = 2$.

q	α_0	6th order WKB (Padé), ($n = 1$)		8th order WKB (Padé), ($n = 1$)	
		$Re(\omega)$	$Im(\omega)$	$Re(\omega)$	$Im(\omega)$
0.0	0.0	0.436533	$-0.290727i$	0.436522	$-0.290724i$
0.2	0.0	0.439932	$-0.291343i$	0.439932	$-0.291343i$
0.2	0.1	0.440478	$-0.290827i$	0.440477	$-0.290827i$
0.4	0.2	0.453322	$-0.290489i$	0.453324	$-0.290491i$
0.6	0.3	0.478945	$-0.28627i$	0.478945	$-0.28627i$
0.8	0.4	0.521604	$-0.256562i$	0.521576	$-0.256573i$

As we can see, Table (I) lists the fundamental-mode QNMs for the massless electromagnetic perturbation ($l = 2$) computed with 6th- and 8th-order WKB with Padé averaging. Both WKB orders produce very similar values for $Re(\omega)$ and $Im(\omega)$, indicating good convergence of the method for these parameters. As the charge q or the BH parameter α_0 is increased, the real part of the frequency shifts upward and the modes oscillate faster while the magnitude of the imaginary part decreases, i.e., modes begin to damp more slowly, and thus the damping times lengthen. The table therefore demonstrates that introducing charge and parameter stiffen the effective potential and prolong the decay time of the fundamental electromagnetic mode.

Similarly, Table (II) reports the first overtone ($n = 1$) for the electromagnetic field at $l = 2$. The overtone be-

haves qualitatively like the fundamental mode with respect to q and α_0 (increasing $Re(\omega)$ and decreasing the absolute damping), but it displays the expected overtone characteristics: relative to the fundamental the overtone is more strongly damped (more negative $Im(\omega)$) and shows slightly greater sensitivity to the WKB order. This increased sensitivity for $n = 1$ is a known property of WKB approaches and is visible here as marginally larger differences between the 6th- and 8th-order Padé results compared with the fundamental.

In Table (III) we compute the fundamental electromagnetic QNMs for $l = 3$. Compared with the $l = 2$ fundamental (Table I), higher multipole index results in larger $Re(\omega)$ and a larger magnitude of $Im(\omega)$, consistent with a steeper and narrower effective potential at larger l . The dependence on q and α_0 follows the same

TABLE III. Quasinormal mode frequencies ω for the massless electromagnetic field perturbations for the fundamental mode ($n = 0$), obtained using the 6th and 8th order WKB methods with Padé Averaging for various values of q and α_0 . We set $M = 1$ and $l = 3$.

q	α_0	6th order WKB (Padé), ($n = 0$)		8th order WKB (Padé), ($n = 0$)	
		$Re(\omega)$	$Im(\omega)$	$Re(\omega)$	$Im(\omega)$
0.0	0.0	0.656899	$-0.0956163i$	0.656899	$-0.0956162i$
0.2	0.0	0.661439	$-0.0958322i$	0.661439	$-0.0958324i$
0.2	0.1	0.66199	$-0.0956758i$	0.66199	$-0.0956758i$
0.4	0.2	0.678516	$-0.0956705i$	0.678516	$-0.0956705i$
0.6	0.3	0.711544	$-0.0945891i$	0.711544	$-0.0945891i$
0.8	0.4	0.778514	$-0.0852404i$	0.778515	$-0.0852402i$

TABLE IV. Quasinormal mode frequencies ω for the massless electromagnetic field perturbations for the first overtone ($n = 1$), obtained using the 6th and 8th order WKB methods with Padé Averaging for various values of q and α_0 . We set $M = 1$ and $l = 3$.

q	α_0	6th order WKB (Padé), ($n = 1$)		8th order WKB (Padé), ($n = 1$)	
		$Re(\omega)$	$Im(\omega)$	$Re(\omega)$	$Im(\omega)$
0.0	0.0	0.641736	$-0.289731i$	0.641735	$-0.28973i$
0.2	0.0	0.646396	$-0.290355i$	0.646396	$-0.290354i$
0.2	0.1	0.647034	$-0.289862i$	0.647034	$-0.289862i$
0.4	0.2	0.664249	$-0.289673i$	0.664249	$-0.289674i$
0.6	0.3	0.698578	$-0.285969i$	0.698578	$-0.285969i$
0.8	0.4	0.762154	$-0.257542i$	0.762149	$-0.257543i$

pattern seen before: raising either parameter increases the oscillation frequency and reduces the damping magnitude. Agreement between the 6th- and 8th-order Padé-averaged WKB remains close, supporting numerical stability for these higher multipoles in the parameter ranges shown. The first overtone for $l = 3$ in Table (IV) again shows the canonical overtone features, it is more strongly damped and typically has a somewhat different real and imaginary parts compared to $n = 0$. Parameter trends with respect to q and α_0 remain consistent with the the analysis of the previous tables.

In Table (V) we list fundamental modes for massless Dirac perturbations with $|k| = 2$. Qualitatively the Dirac spectrum mirrors the electromagnetic case: increasing q or α_0 pushes $Re(\omega)$ upward and makes $Im(\omega)$ less negative, i.e. oscillations become faster and longer-lived as the parameters increase. The 6th- and 8th-order WKB–Padé results are in close agreement for the fundamental Dirac

mode, indicating that the chosen WKB orders are sufficiently accurate for these modes and parameter ranges, and similarly, we have Table (VI) where the first overtone of the Dirac field at $|k| = 2$ shows that overtone pattern, i.e, the real part of the frequencies is slightly lower than $n = 0$ case. The parameter dependence is consistent with the other tables; both q and α_0 reduce damping magnitude and increase oscillation frequency. Practically, this means Dirac overtones also become longer lived and somewhat higher in frequency with increased charge or the BH parameter.

Finally we have the Table (VII) for Dirac perturbations at $|k| = 3$ (fundamental) both the real and imaginary parts are larger in magnitude compared to $|k| = 2$, consistent with the multipole hierarchy: larger angular index corresponds to a higher frequency, faster decaying response. The monotone trends with q and α_0 persist here as well. The 6th- and 8th-order WKB–Padé columns

TABLE V. Quasinormal mode frequencies ω for the massless Dirac field perturbations for the fundamental mode ($n = 0$), obtained using the 6th and 8th order WKB methods with Padé Averaging for various values of q and α_0 . We set $M = 1$ and $|k| = 2$.

q	α_0	6th order WKB (Padé), ($n = 0$)		8th order WKB (Padé), ($n = 0$)	
		$Re(\omega)$	$Im(\omega)$	$Re(\omega)$	$Im(\omega)$
0.0	0.0	0.380054	$-0.0963853i$	0.380051	$-0.0963904i$
0.2	0.0	0.38268	$-0.0965934i$	0.382675	$-0.0966004i$
0.2	0.1	0.382981	$-0.0964316i$	0.382977	$-0.0964365i$
0.4	0.2	0.392473	$-0.096383i$	0.392468	$-0.0963857i$
0.6	0.3	0.411318	$-0.0951834i$	0.411291	$-0.095181i$
0.8	0.4	0.447367	$-0.0859194i$	0.447366	$-0.0859201i$

TABLE VI. Quasinormal mode frequencies ω for the massless Dirac field perturbations for the first overtone ($n = 1$), obtained using the 6th and 8th order WKB methods with Padé Averaging for various values of q and α_0 . We set $M = 1$ and $|k| = 2$.

q	α_0	6th order WKB (Padé), ($n = 1$)		8th order WKB (Padé), ($n = 1$)	
		$Re(\omega)$	$Im(\omega)$	$Re(\omega)$	$Im(\omega)$
0.0	0.0	0.355778	$-0.297269i$	0.355769	$-0.297303i$
0.2	0.0	0.35858	$-0.297826i$	0.358571	$-0.297842i$
0.2	0.1	0.359029	$-0.297324i$	0.359024	$-0.297324i$
0.4	0.2	0.369693	$-0.29662i$	0.369687	$-0.296612i$
0.6	0.3	0.390698	$-0.29152i$	0.390255	$-0.29184i$
0.8	0.4	0.41957	$-0.262825i$	0.419348	$-0.263346i$

remain in good agreement, reinforcing confidence in the computed fundamental-mode values at these multipoles.

The first overtone for $|k| = 3$ in Table (VIII) exhibits the standard behavior relative to the fundamental: increased damping and a characteristic shift of the real part consistent with overtone structure. Here it is observed that increasing q or α_0 slightly lowers the oscillation frequency and reduces the damping magnitude. Differences between 6th- and 8th-order results are slightly larger here than for fundamentals, but do not change the qualitative conclusions drawn from the table.

Across all Tables, the QNM spectra exhibit a clear and consistent pattern: the real part of the frequency $Re(\omega)$ increases with both the electric charge q and the regularization parameter α_0 , while the imaginary part $Im(\omega)$ becomes less negative, indicating slower damping and longer-lived perturbations. Increasing the angular index (l or $|k|$) raises both the oscillation frequency and

the damping magnitude. The close agreement between the 6th- and 8th-order WKB–Padé results for the fundamental modes confirms the reliability and numerical stability of the method, while the expected mild sensitivity for higher overtones remains within acceptable limits. These results suggest that the inclusion of charge and parameter effects modifies the effective potential of the underlying BH geometry, producing higher frequencies and longer lived oscillations.

It is important to note that in the present analysis, we have restricted our computations to the modes satisfying $n < l$ (or $n < |k|$ for Dirac perturbations) and have not considered the special case $l = n = 0$, since the WKB method is applicable only when $l \geq n$. Furthermore, for higher overtone numbers ($n \geq l$), the WKB method progressively loses accuracy due to the breakdown of the eikonal approximation and the increasing influence of the inner potential well at smaller radii. In such regimes, more robust numerical approaches such as time-domain

TABLE VII. Quasinormal mode frequencies ω for the massless Dirac field perturbations for the fundamental mode ($n = 0$), obtained using the 6th and 8th order WKB methods with Padé Averaging for various values of q and α_0 . We set $M = 1$ and $|k| = 3$.

q	α_0	6th order WKB (Padé), ($n = 0$)		8th order WKB (Padé), ($n = 0$)	
		$Re(\omega)$	$Im(\omega)$	$Re(\omega)$	$Im(\omega)$
0.0	0.0	0.574094	$-0.0963048i$	0.574094	$-0.0963048i$
0.2	0.0	0.578015	$-0.0965155i$	0.578015	$-0.0965156i$
0.2	0.1	0.578467	$-0.0963577i$	0.578467	$-0.0963577i$
0.4	0.2	0.592637	$-0.0963316i$	0.592636	$-0.0963317i$
0.6	0.3	0.620832	$-0.0952188i$	0.620831	$-0.095218i$
0.8	0.4	0.676997	$-0.086072i$	0.676996	$-0.0860717i$

TABLE VIII. Quasinormal mode frequencies ω for the massless Dirac field perturbations for the first overtone ($n = 1$), obtained using the 6th and 8th order WKB methods with Padé Averaging for various values of q and α_0 . We set $M = 1$ and $|k| = 3$.

q	α_0	6th order WKB (Padé), ($n = 1$)		8th order WKB (Padé), ($n = 1$)	
		$Re(\omega)$	$Im(\omega)$	$Re(\omega)$	$Im(\omega)$
0.0	0.0	0.557015	$-0.292715i$	0.557015	$-0.292715i$
0.2	0.0	0.56107	$-0.293314i$	0.561071	$-0.293315i$
0.2	0.1	0.561614	$-0.292812i$	0.561614	$-0.292813i$
0.4	0.2	0.576534	$-0.292511i$	0.576534	$-0.29251i$
0.6	0.3	0.606124	$-0.288564i$	0.606113	$-0.288563i$
0.8	0.4	0.658189	$-0.260521i$	0.658168	$-0.260649i$

integration, continued-fraction (Leaver) methods, or the asymptotic iteration method are required to obtain reliable QNM frequencies. We leave this direction of research for future investigations.

V. GREY-BODY FACTORS

Grey-body factors quantify the fraction of the initial Hawking radiation that successfully transmits through the effective potential barrier surrounding the black hole, rather than being reflected back toward the event horizon. To compute this quantity, we apply Hawking's semi-classical formula, now modified with a grey-body factor, to estimate the radiation flux that reaches a distant observer. This approach is particularly relevant when considering the late stages of black hole evaporation, even when using the metric function (Eq. (2)).

As discussed in the literature, the contribution of gravi-

tons to the total radiation flux is negligible — for instance, in the Schwarzschild case, gravitons account for less than 2% of the emitted radiation [43]. Consequently, grey-body factors for test fields are sufficient to characterize the radiation spectrum. Moreover, these factors can be more influential than the Hawking temperature itself in determining the intensity of the observed flux [44].

To compute the grey-body factors, we analyze the wave equation under scattering boundary conditions that allow for an incident wave from spatial infinity. Owing to the symmetry of the scattering problem, this is equivalent to studying a wave incident from the horizon. The appropriate boundary conditions for the field $\Psi(r_*)$ are given by

$$\Psi(r_*) = \begin{cases} e^{-i\omega r_*} + Re^{i\omega r_*}, & r_* \rightarrow +\infty, \\ Te^{-i\omega r_*}, & r_* \rightarrow -\infty, \end{cases} \quad (28)$$

where R and T are the reflection and transmission coef-

ficients, respectively.

Because the effective potential has a single barrier-like peak and falls off monotonically toward both infinities, the WKB approximation [45] can be reliably applied to compute R and T . Since ω^2 is real, the first-order WKB approximation yields real values for R and T , satisfying

$$|T|^2 + |R|^2 = 1. \quad (29)$$

From the reflection coefficient, the transmission coefficient for each multipole number ℓ can be obtained as

$$|A_\ell|^2 = 1 - |R_\ell|^2 = |T_\ell|^2, \quad (30)$$

where A_ℓ represents the grey-body factor.

In our analysis, we employ the higher-order WKB formula [37, 38] to obtain a precise estimate of the reflection and transmission coefficients. This approach, however, becomes unreliable at very low frequencies, where almost all of the wave is reflected and the contribution to the total energy flux is negligible. In this regime, we follow the standard approach of extrapolating the WKB result to small ω .

According to Refs. [36, 45], the reflection coefficient takes the form

$$R = (1 + e^{-2i\pi K})^{-1/2}, \quad (31)$$

where K is determined from the equation

$$K - i \frac{\omega^2 - V_{\max}}{\sqrt{-2V''_{\max}}} - \sum_{i=2}^6 \Lambda_i(K) = 0. \quad (32)$$

Here, V_{\max} and V''_{\max} are the value and second derivative of the effective potential at its peak, while $\Lambda_i(K)$ denote the higher-order WKB correction terms. It is worth noting that the WKB expansion is asymptotic rather than convergent, and there usually exists an optimal order at which the accuracy is maximal. The appropriate order depends sensitively on the shape of the effective potential. Here we used the 6th order approximation and 3rd order approximation for calculating grey-body factors.

VI. UNRUH TEMPERATURE

In this section we examine the Unruh temperature associated with the spacetime under consideration. This temperature reflects the surface gravity or, equivalently, the proper acceleration felt by an observer stationed at

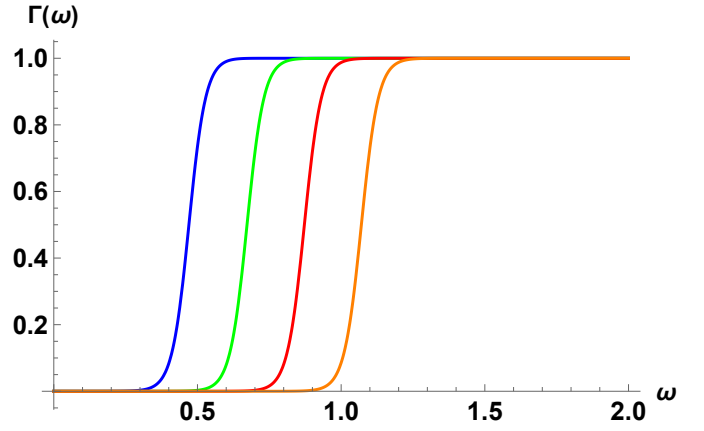


FIG. 8. Grey-body factors of the massless electromagnetic field as a function of frequency for the Frolov black hole with $l = 2, 3, 4, 5$ (from left to right) and $\alpha_0 = 0.4$ and $q = 0.2$.

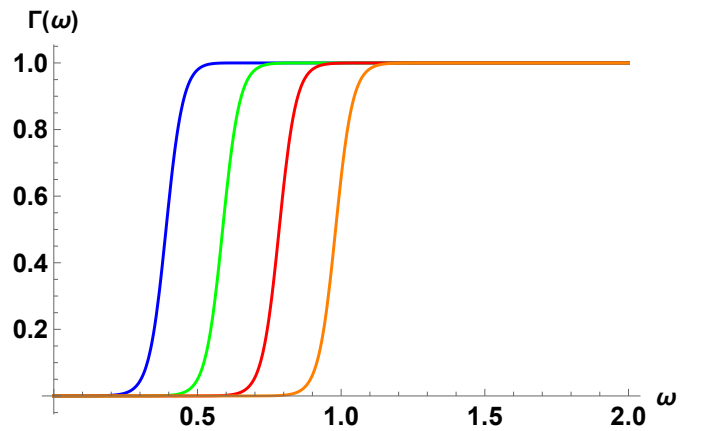


FIG. 9. Grey-body factors of the Dirac field as a function of frequency for the Frolov black hole with $|k| = 2, 3, 4, 5$ (from left to right) and $\alpha = 0.4$ and $q = 0.2$.

a fixed radial distance from the black hole. Such a property has also been explored in various alternative theories of gravity. The Unruh temperature can be expressed in terms of the red-shifted surface gravity, or more generally through covariant quantities involving the gravitational potential and the timelike Killing vector field. Previously, the Unruh temperature has been investigated in various setups [46, 47].

Let ϕ denote the gravitational potential and ξ^α a timelike Killing vector. The potential is defined as

$$\phi = \frac{1}{2} \ln[-g_{\alpha\beta} \xi^\alpha \xi^\beta]. \quad (33)$$

Here e^ϕ represents the red-shift factor, which approaches unity at spatial infinity because $\phi = 0$ as $r \rightarrow \infty$, provided the spacetime is asymptotically flat.

The background geometry is assumed to be a static solution that admits a global timelike Killing vector ξ^α .

The local acceleration then follows from

$$a^\alpha = -g^{\alpha\beta}\nabla_\beta\phi. \quad (34)$$

The corresponding Unruh temperature is

$$T_{\text{Unruh}} = \frac{\hbar}{2\pi} e^\phi n_\alpha \nabla^\alpha \phi, \quad (35)$$

Here n^α is a unit vector that is everywhere orthogonal to the timelike Killing vector ξ^α . This equation can be rewritten using eq.(33) as [48]

$$T_{\text{Unruh}} = \frac{\hbar}{2\pi} e^\phi \sqrt{g^{\alpha\beta} \partial_\alpha \phi \partial_\beta \phi}. \quad (36)$$

For a static, spherically symmetric black hole with metric function $f(r)$, a static observer at radius r measures by setting $\hbar = 1$, and $M = 1$ this becomes,

$$T(r) = \frac{r (q^4 \alpha^2 + Mr^2 (r^3 - 4M\alpha^2) - q^2 (r^4 + 2Mra^2))}{2\pi (r^4 + q^2 \alpha^2 + 2Mra^2)^2} \quad (37)$$

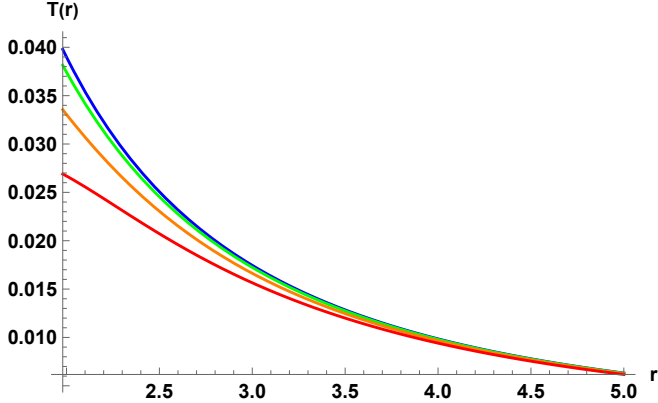


FIG. 10. Unruh temperature as a function of the radial coordinate for $M = 1$ and fixed $q = 0.2$ with $\alpha_0 = 0$ (blue), $\alpha_0 = 0.2$ (green), $\alpha_0 = 0.4$ (orange), and $\alpha_0 = 0.6$ (red).

Figures (10) and (11) depict the variation of the Unruh–Verlinde temperature $T(r)$ with respect to the radial coordinate r for the Frolov black hole. In both cases, the temperature exhibits a monotonically decreasing behavior with increasing r , approaching zero asymptotically. This trend is consistent with the expectation that the effective temperature perceived by a static observer

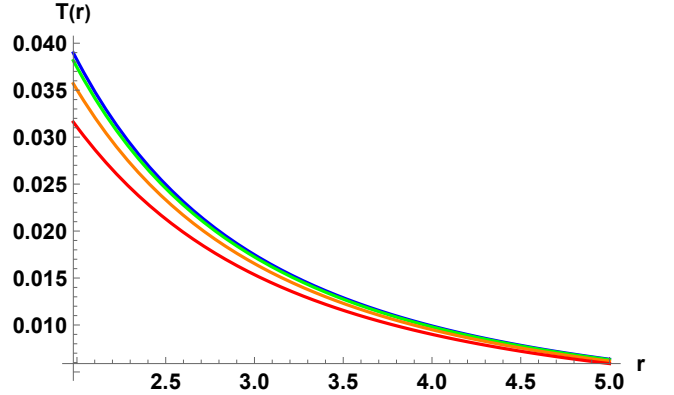


FIG. 11. Unruh temperature as a function of the radial coordinate for $M = 1$ and fixed $\alpha_0 = 0.2$ with $q = 0$ (blue), $q = 0.2$ (green), $q = 0.4$ (orange) and $q = 0.6$ (red).

decreases with distance from the gravitational source due to the redshift of local acceleration.

In Fig.(10), the BH parameter α_0 is varied while keeping the charge fixed. Similar to the effect of q , increasing α_0 also lowers the Unruh temperature profile. It can be seen that a larger α_0 weakens the spacetime curvature near the core, reducing the surface gravity at the horizon and hence the temperature. This behavior indicates that the inclusion of parameter effects leads to a more stable and colder black hole configuration.

In Fig.(11), the charge parameter q is varied while keeping the regularization parameter $\alpha_0 = 0.2$ fixed. It can be seen that increasing q leads to a systematic decrease in the Unruh temperature across the entire radial domain. The presence of electric charge effectively weakens the gravitational attraction experienced by a static observer, resulting in a reduced proper acceleration and, consequently, a lower Unruh temperature. The curves clearly demonstrate that the black hole becomes thermodynamically "cooler" as the charge grows, approaching the extremal limit where $T \rightarrow 0$.

Both parameters q and α_0 act to suppress the Unruh–Verlinde temperature. The temperature profiles confirm that the Frolov black hole smoothly interpolates between the classical Schwarzschild case ($q = 0$, $\alpha_0 = 0$) and a regularized, cooler configuration where parameter corrections and charge effects dominate.

VII. DISCUSSION AND CONCLUSIONS

We have carried out a detailed study of the quasinormal modes (including the first overtone), grey-body factors, and Unruh temperature for test electromagnetic and Dirac fields propagating in the background of a static charged regular black hole, also known as the Frolov BH, arising in Quantum Gravity scenarios. Using the sixth-order WKB approximation for the electromagnetic field and for the Dirac field we cross-checked with higher-order approximations and Padé Averaging for numerical consistency and derived and solved the corresponding wave equations for both cases.

The QNM spectra of the Frolov black hole, obtained in this case, reveal distinct features that set this regularized geometry apart from the classical Schwarzschild and Reissner–Nordström (RN) spacetimes. For all modes considered, the real part of the frequency $Re(\omega)$ increases with both the electric charge q and the BH parameter α_0 , indicating that the inclusion of these parameters strengthens the effective potential barrier and raises the oscillation frequency of perturbations. Simultaneously, the magnitude of the imaginary part $|Im(\omega)|$ decreases, showing that damping becomes weaker and the perturbations persist longer.

The excellent agreement between the sixth and eighth-order WKB–Padé averaged results confirms the reliability of the computed spectra for both fundamental and overtone modes. The standard multipole and overtone hierarchies are preserved—higher l (or $|k|$) leads to larger $Re(\omega)$ and stronger damping, while higher n corresponds to faster decay which shows that the fundamental structure of the perturbative response remains intact. One can infer clearly from the tables how the spectra differs from the standard results of the Schwarzschild ($q = 0$ and $\alpha_0 = 0$) as well as the Reissner–Nordström case ($\alpha_0 = 0$). These findings establish that the Frolov spacetime suggest that its ringdown signature could provide a distinct observational imprint of quantum-gravity inspired reg-

ular black holes. The grey-body factors, which determine the transmission probability of Hawking radiation through the effective potential barrier, are also affected by the corrections. We find that quantum effects slightly suppress the transmission coefficients at lower frequencies, effectively modifying the spectrum of radiation that reaches a distant observer. This suppression reflects how the modified spacetime geometry alters the scattering properties of the black hole potential.

In addition, our results indicate that the Unruh temperature decreases monotonically with increasing α_0 while fixing the charge q and vice versa, suggesting a direct influence of these corrections on the thermal properties of the horizon. These findings highlight that while QNM ringing remains a robust observable for probing strong-field regimes and constraining possible quantum gravity effects. Our analysis opens up several avenues for future investigation. It would be particularly interesting to extend this work by studying the gravitational perturbations in greater detail, as such modes are directly linked to the quasinormal spectra observable in future gravitational wave detections. A comprehensive analysis incorporating both axial and polar perturbations would help to establish the complete dynamical stability of the Frolov black hole spacetime. Furthermore, it would be valuable to explore the Hawking radiation spectra associated with this geometry, as well as to investigate its implications in the context of modified theories of gravity and quantum gravitational corrections.

ACKNOWLEDGMENTS

The author is thankful to R.A Konoplya for useful discussions and for suggesting improvements on the draft. The author also expresses his gratitude to Pankaj S. Joshi and Parth Bambhaniya for giving the opportunity to visit ICSC, Ahmedabad University.

[1] R. Penrose, [Phys. Rev. Lett. **14**, 57-59 \(1965\)](#)
[2] S. W. Hawking, [Phys. Rev. Lett. **17**, 444-445 \(1966\)](#)
[3] Valeri P. Frolov. Remarks on non-singular black holes. *EPJ Web Conf.*, 168:01001, 2018. doi: [10.1051/epjconf/201816801001](https://doi.org/10.1051/epjconf/201816801001).
[4] E. Ayon-Beato and A. Garcia, [Phys. Lett. B **493**, 149-152 \(2000\)](#) [[arXiv:gr-qc/0009077](https://arxiv.org/abs/gr-qc/0009077) [gr-qc]].
[5] I. Dymnikova, [Class. Quant. Grav. **21**, 4417-4429 \(2004\)](#) [[arXiv:gr-qc/0407072](https://arxiv.org/abs/gr-qc/0407072) [gr-qc]].

[6] I. Dymnikova. Vacuum nonsingular black hole. *General Relativity and Gravitation*, 24:235–242, 1992. doi: 10.1007/BF00760226.

[7] S. Ansoldi, [arXiv:0802.0330 [gr-qc]].

[8] J. Ovalle, *Phys. Rev. D* **109**, no.10, 104032 (2024) [arXiv:2405.06731 [gr-qc]].

[9] J. Ovalle, [arXiv:2509.00816 [gr-qc]].

[10] J. P. S. Lemos and V. T. Zanchin, *Phys. Rev. D* **83**, 124005 (2011) [arXiv:1104.4790 [gr-qc]].

[11] S. A. Hayward, *Phys. Rev. Lett.* **96**, 031103 (2006) [arXiv:gr-qc/0506126 [gr-qc]].

[12] V. P. Frolov, *Phys. Rev. D* **94**, no.10, 104056 (2016) [arXiv:1609.01758 [gr-qc]].

[13] L. Xiang, Y. Ling and Y. G. Shen, *Int. J. Mod. Phys. D* **22**, 1342016 (2013) [arXiv:1305.3851 [gr-qc]].

[14] H. Culetu, [arXiv:1305.5964 [gr-qc]].

[15] H. Culetu, *Int. J. Theor. Phys.* **54**, no.8, 2855–2863 (2015) [arXiv:1408.3334 [gr-qc]].

[16] M. E. Rodrigues, E. L. B. Junior, G. T. Marques and V. T. Zanchin, *Phys. Rev. D* **94**, no.2, 024062 (2016) [arXiv:1511.00569 [gr-qc]].

[17] A. Simpson and M. Visser, *Universe* **6**, no.1, 8 (2019) [arXiv:1911.01020 [gr-qc]].

[18] S. G. Ghosh, *Eur. Phys. J. C* **75**, no.11, 532 (2015) [arXiv:1408.5668 [gr-qc]].

[19] X. Li, Y. Ling, Y. G. Shen, C. Z. Liu, H. S. He and L. F. Xu, *Annals Phys.* **396**, 334–350 (2018) [arXiv:1611.09016 [gr-qc]].

[20] M. Martinis and N. Perkovic, [arXiv:1009.6017 [gr-qc]].

[21] Y. Ling and M. H. Wu, *Class. Quant. Grav.* **40**, no.7, 075009 (2023) [arXiv:2109.05974 [gr-qc]].

[22] R. A. Konoplya and A. Zhidenko, *Rev. Mod. Phys.* **83**, 793–836 (2011) [arXiv:1102.4014 [gr-qc]].

[23] E. Berti, V. Cardoso and A. O. Starinets, *Class. Quant. Grav.* **26**, 163001 (2009) [arXiv:0905.2975 [gr-qc]].

[24] R. A. Konoplya and A. Zhidenko, *JCAP* **09**, 068 (2024) [arXiv:2406.11694 [gr-qc]].

[25] C. Tang, Y. Ling and Q. Q. Jiang, ”Correspondence between grey-body factors and quasinormal modes for regular black holes with sub-Planckian curvature,” .

[26] S. V. Bolokhov and M. Skvortsova, *JCAP* **04**, 025 (2025) [arXiv:2412.11166 [gr-qc]].

[27] A. Dubinsky, *International Journal of Gravitation and Theoretical Physics*, **1**, 2 (2025)

[28] R. A. Konoplya, *Phys. Lett. B* **823**, 136734 (2021) [arXiv:2109.01640 [gr-qc]].

[29] Z. Song, H. Gong, H. L. Li, G. Fu, L. G. Zhu and J. P. Wu, *Commun. Theor. Phys.* **76**, no.10, 105401 (2024) [arXiv:2406.04787 [gr-qc]].

[30] L. A. Lopez and V. Hinojosa, *Can. J. Phys.* **99**, no.1, 44–48 (2021) [arXiv:1810.09034 [gr-qc]].

[31] K. G. Arun *et al.* [LISA], *Living Rev. Rel.* **25**, no.1, 4 (2022) [arXiv:2205.01597 [gr-qc]].

[32] E. Barausse, E. Berti, T. Hertog, S. A. Hughes, P. Jetzer, P. Pani, T. P. Sotiriou, N. Tamanini, H. Witek and K. Yagi, *et al.* *Gen. Rel. Grav.* **52**, no.8, 81 (2020) [arXiv:2001.09793 [gr-qc]].

[33] C. DeWitt and B. S. DeWitt, R. Ruffini, in *Black Hole: les Astres Occlus* (Gordon and Breach New York, 1973) Proceedings, Ecole d’Eté de Physique Théorique: Les Astres Occlus: Les Houches, France, August, 1972,”

[34] J. Li, M. Hong and K. Lin, *Phys. Rev. D* **88**, 064001 (2013) [arXiv:1308.6499 [gr-qc]].

[35] B. F. Schutz and C. M. Will, *APJL* **291**, L33–L36, (1985).

[36] S. Iyer and C. M. Will, *Phys. Rev. D* **35**, 3621–3631, (1987)..

[37] R. A. Konoplya, A. Zhidenko and A. F. Zinhailo, *Class. Quant. Grav.* **36**, 155002 (2019) [arXiv:1904.10333 [gr-qc]].

[38] J. Matyjasek and M. Opala, *Phys. Rev. D* **96**, no.2, 024011 (2017) [arXiv:1704.00361 [gr-qc]].

[39] Y. Hatsuda, *Phys. Rev. D* **101**, no.2, 024008 (2020) [arXiv:1906.07232 [gr-qc]].

[40] R. Konoplya, “Mathematica R package for QNM and grey-body factor calculations,” available at: <https://goo.gl/nykYGL>.

[41] K. D. Kokkotas and B. G. Schmidt, *Living Rev. Rel.* **2**, 2 (1999) [arXiv:gr-qc/9909058 [gr-qc]].

[42] J. Matyjasek and M. Telecka, *Phys. Rev. D* **100**, no.12, 124006 (2019) [arXiv:1908.09389 [gr-qc]].

[43] D. N. Page, *Phys. Rev. D* **13**, 198–206 (1976)

[44] R. A. Konoplya and A. F. Zinhailo, *Phys. Rev. D* **99**, no.10, 104060 (2019) [arXiv:1904.05341 [gr-qc]].

[45] R. A. Konoplya, *Phys. Rev. D* **68**, 024018 (2003) [arXiv:gr-qc/0303052 [gr-qc]].

[46] E. P. Verlinde, *JHEP* **04**, 029 (2011) [arXiv:1001.0785 [hep-th]].

[47] R. A. Konoplya, *Eur. Phys. J. C* **69**, 555–562 (2010) [arXiv:1002.2818 [hep-th]].

[48] W. G. Unruh, *Phys. Rev. D* **14**, 870 (1976)